Article
Vol. 25, No. 6, p. 877–890, December 2021
https://doi.org/10.1007/s12303-021-0021-7
pISSN 1226-4806 eISSN 1598-7477
Geosciences Journal GJ

Time-lapse electrical resistivity tomography and ground penetrating radar mapping of the active layer of permafrost across a snow fence in Cambridge Bay, Nunavut Territory, Canada: correlation interpretation using vegetation and meteorological data

Kwansoo Kim[1,2], Joohan Lee[1], Hyeontae Ju[1], Ji Young Jung[1], Namyi Chae[3], Junhwa Chi[1], Min Jung Kwon[1†], Bang Yong Lee[1], Johann Wagner[4], and Ji-Soo Kim[2*]

[1]Korea Polar Research Institute, Incheon 21990, Republic of Korea
[2]Department of Earth and Environmental Sciences, Chungbuk National University, Cheongju 28644, Republic of Korea
[3]Institutes of Life Sciences and Natural Resources, Korea University, Seoul 02841, Republic of Korea
[4]Polar Knowledge Canada, 1 Uvajuq Road, Cambridge Bay, PO Box 2150, NU X0B 0C0, Canada

ABSTRACT: The active layer thickness (ALT) is a key parameter for permafrost studies. Changes in the ALT are affected mainly by air and ground temperatures, physical and thermal properties of the surface and subsurface materials, soil moisture, vegetation, and the duration and thickness of snow cover. Ground penetrating radar (GPR) and electrical resistivity tomography (ERT) were employed across a snow fence during the thawing season to delineate and monitor the active layer of permafrost in Cambridge Bay, Nunavut, Canada. The variation of the ALT is well captured by the high-resolution time-lapse radargram. At the position of the fence, the active layer thickens over the thawing period from 0.5 m depth at the beginning to 1.0 m depth at the end. The active layer is thicker in the pre-fence area (C zone) than in the post-fence area (H zone). As the air temperature increases with time, the difference in thickness between the two zones decreases, eventually becoming almost equal. Changes in the ALT are represented in the ERT by low resistivities (< 200 Ωm), which decrease gradually with time. This occurs most significantly in the H zone due to the rapidly increasing temperature in the absence of snow cover. The electrical resistivity structure of the active layer is well correlated with the vegetation activity, as measured by the normalized difference vegetation index, air/ground temperatures, soil moisture, snow cover, and snow accumulation controlled by the fence. Geophysical data interpretation and correlation schemes with vegetation and meteorological data explored in this paper can be applied to monitor the active layer, which is expected to thin during the freezing season.

Key words: snow fence, geophysical survey, active layer, normalized difference vegetation index (NDVI), permafrost

Manuscript received April 6, 2021; Manuscript accepted July 2, 2021

1. INTRODUCTION

Permafrost, ground that remains at or below 0 °C for more than two consecutive years, consists of soil, rock, embedded ice, and organic materials. It occupies approximately 22% of the land surface in the Northern Hemisphere (Brown et al., 1997). Continuous permafrost, which underlays 90% or more of the ground, is usually only absent beneath rivers and lakes that do not freeze to the bottom in winter. At warmer temperatures, variations due to microclimatic effects lead to a zone of widespread discontinuous permafrost underlying 50–90% of the ground (Osterkamp and Burn, 2003).

The active layer is defined as the layer of ground that is subject to annual thawing and freezing in areas underlain by permafrost. It plays an important role in cold regions of the Earth, due to its internal ecological, hydrological, biochemical, pedogenic, and

*Corresponding author:
Ji-Soo Kim
Department of Earth and Environmental Sciences, Chungbuk National University, Cheongju 28644, Republic of Korea
Tel: +82-43-261-3201, Fax: +82-43-276-9645,
E-mail: geop22@chungbuk.ac.kr
†Present address: Le Laboratoire des Sciences du Climat et de l'Environnement, Gif-sur-Yvette 91190, France

geomorphic processes (Woo, 2012), and is responsible for water and heat exchange between the lithosphere and the atmosphere. The thickness of the active layer is therefore of considerable importance for studies of permafrost terrain and has typically been investigated in terms of meteorological data (air temperature, soil temperature, and moisture), snowfall, rainfall, and vegetation coverage. The active layer plays an especially critical role in the carbon cycle, in that it allows vegetation at high latitudes to accumulate carbon in terrestrial ecosystems during the growing season, which is shorter than that at lower latitudes. In other words, a long period of frozen soil inhibits carbon decomposition, and this has resulted in the accumulation of over 1000 Pg C of soil organic carbon (Hugelius et al., 2014; Schuur et al., 2015), and is vulnerable to future climate change (Blanc-Betes et al., 2016; Pries et al., 2016).

To determine the active layer thickness (ALT), traditional methods such as mechanical probing and temperature measurement have been used. However, those methods can only obtain one-dimensional single data points. In the 2000s, a number of geophysical surveys were conducted to obtain two-dimensional data coverage of the physical properties (e.g., thermal properties, electric and dielectric properties, and seismic velocity) of underground materials (Briggs et al., 2017; Farzamian et al., 2020).

During the process of active-layer thawing, the addition of soil water from both snowmelt and vegetation cover has a great influence on the ALT; therefore, the snow depth and vegetation cover are closely related. Snowfall strongly influences the soil temperature, moisture, and plant-growing period, ultimately playing an important role in carbon dioxide assimilation. Since the 2000s, there have been some practical studies that have meticulously investigated the relationship between vegetation cover and snow depth by constructing a snow fence to control the snow height (Wipf and Rixen, 2010; Lafreniere et al., 2012; O'Neill and Burn, 2017). These experiments have assessed (1) the thawing period of the ground, (2) the soil temperature and moisture, and (3) the vegetation growth pattern (Wang et al., 2017).

Ground penetrating radar (GPR) and electrical resistivity tomography (ERT) are useful geophysical methods for imaging the bottom of the active layer (i.e., the top of the permafrost; Osterkamp et al., 1980; Harris et al., 1988; Dolbinski, 2009; Erji et al., 2016). In this study, we investigate the variation of the ALT using GPR and ERT at a permafrost site in Cambridge Bay, Nunavut territory, Canada, and its correlation with meteorological data (air temperature, soil temperature, and moisture), snowfall, and the normalized difference vegetation index (NDVI). A geophysical survey passing through a snow fence is also conducted. The snow fence is erected at a right angle to the prevailing wind, which is measured ~100 m away from the fence. Two air temperature profiles for Period I (September 2017–August 2018) and Period II (September 2018–August 2019) are considered when correlating the snow accumulation with the time-lapse ERT/GPR images, ground temperature/moisture, and vegetation activity across the fence.

2. STUDY SITE AND SNOW FENCE

2.1. Site Location and Description

In Nunavut, more than 90% of the land area is underlain by permafrost; unfrozen ground 'taliks' are restricted to the margins of large waterbodies (rivers or lakes) that are deep enough to resist freezing to their bottoms. The maximum thickness of permafrost is largely unknown, but it can reach depths of 500 m on the neighboring island (Taylor et al., 2006).

Most of the eastern part of the island is underlain by generally flat-lying middle Cambrian to upper Silurian carbonates and unconformably overlying terrestrial and marine upper Precambrian sedimentary rocks. Deformed rocks of the Shaler Group lie to the northwest and in the Wellington Inlier west of Cambridge Bay (Harrison et al., 2013). The Eastern Victoria Island and adjacent mainland Nunavut were repeatedly glaciated throughout the Pleistocene by the northwestern edge of the Laurentide Ice Sheet (Barendregt et al., 1998). During the last glacial maximum (24–20 ka BP), all of the northern mainland of Nunavut and Victoria Island were covered by the Laurentide Ice Sheet (McLennan et al., 2015).

Our study area is located in the Cambridge Bay region (69°07′N, 105°04′W), southeastern Victoria Island, Nunavut, Canada (Fig. 1). The elevation is 12 m. The site is ~1 km away from the campus of the Canadian High Arctic Research Station (CHARS), which was established to optimize innovation in Arctic science and technology, and to provide researchers with the technical services they need. The station is entirely within the zone of continuous permafrost (Heginbottom et al., 1995). The research area is mostly flat with well-developed ice wedges. Many lakes formed by thermokarst have been created over time (Frédéric et al., 2020). The mainland is composed of till veneers and blankets which are interbedded in places with sand and gravel. West-trending drumlins, flutings, eskers, and moraines are found northeast of Cambridge Bay (Storrar and Stokes, 2007). Flutings are present locally where drift is thin (1–2 m), and drumlins occur where drift is thick (10–15 m; John, 1980). The active layer is generally interpreted to be less than 1 m thick in the CHARS Greater Ecosystem (McLennan et al., 2015).

2.2. Snow Fence, C zone, and H zone

A snow fence is used as a barrier that forces windblown,

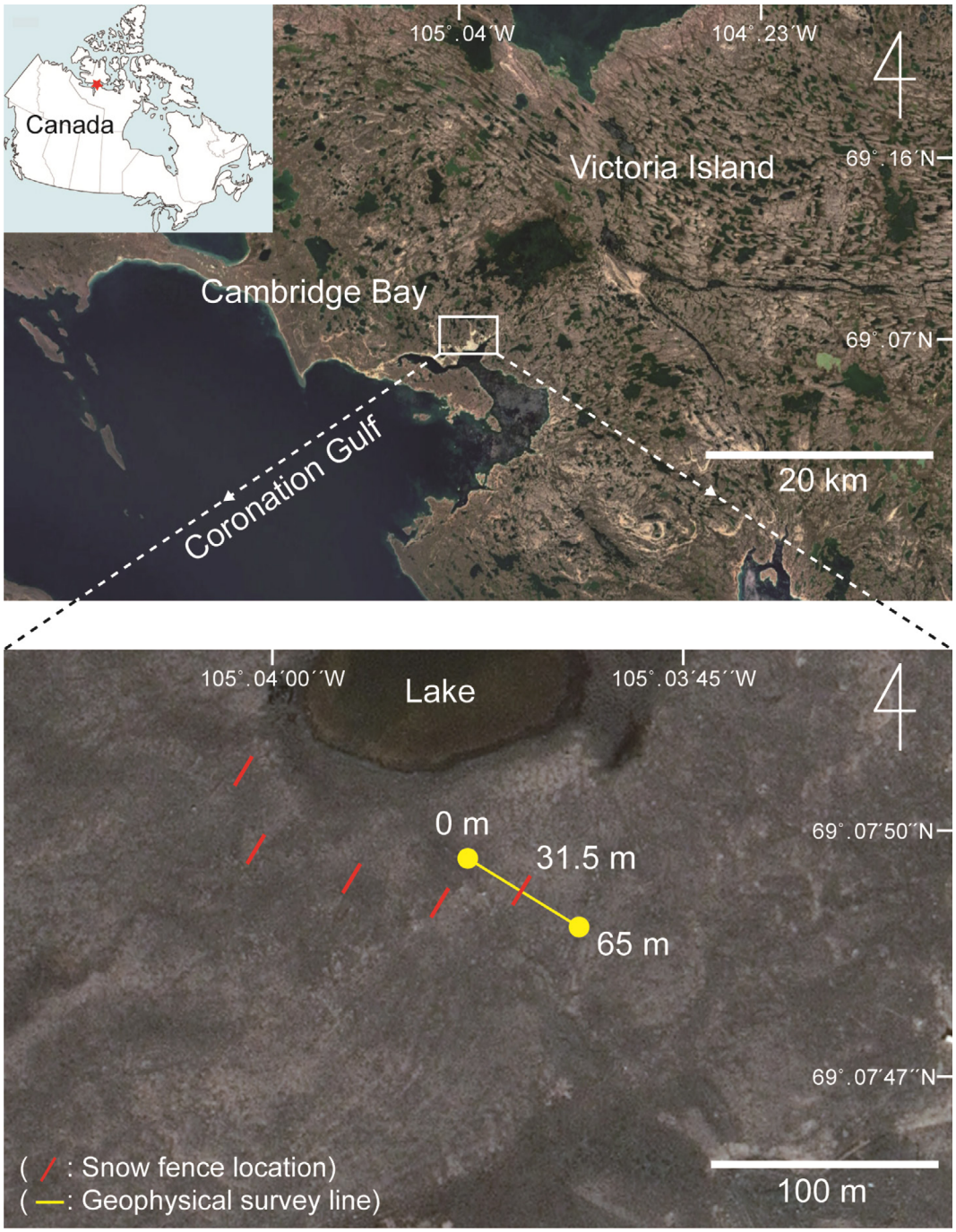

Fig. 1. Study site showing the locations of geophysical survey lines and five snow fences at a permafrost terrain of Cambridge Bay, Nunavut, Canada (modified from Google Maps).

drifting snow to accumulate in a desired place. It is constructed mainly to reduce wind velocity and snow accumulation near the fence in heavy snow regions such as at high elevations in the middle latitudes (e.g., the Alps) and in the Northern Hemisphere at high latitudes (e.g., Alaska). Steep high-altitude areas experience frequent avalanches due to large amounts of snow and strong winds, thus snow fences have been constructed to prevent snowballs from rolling downward. In addition, snow fences are frequently placed along highways in the Northern Hemisphere at high latitudes in order to control the amount of snow accumulation on the road, especially in remote areas (Hinkel and Hurd, 2006).

The windward side at more than 9 m away from the fence is defined as the Control zone (expressed hereafter as "C zone"), where the snow accumulation is not influenced by the fence. The zone 1–6 m away from the fence on the leeward side is

https://doi.org/10.1007/s12303-021-0021-7

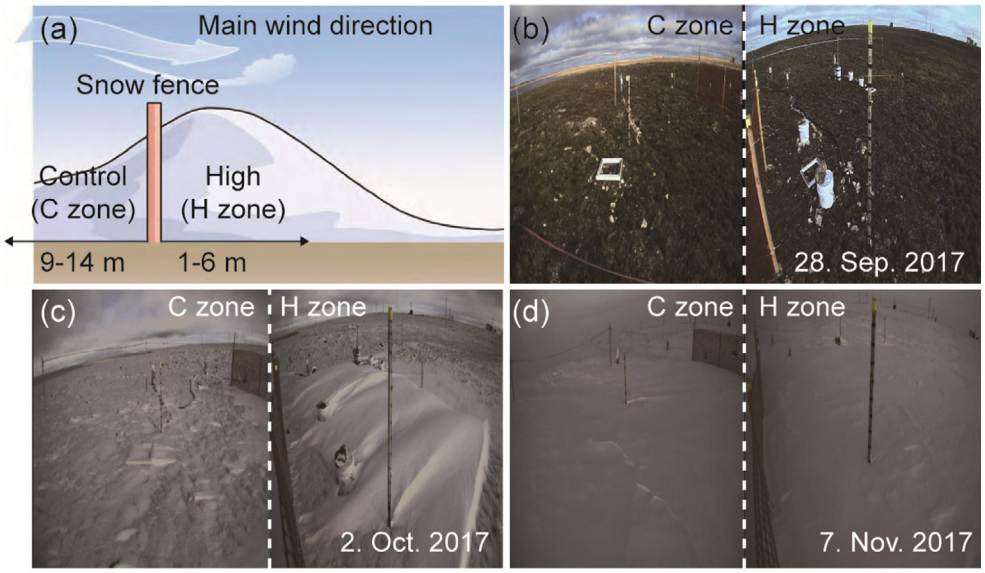

Fig. 2. (a) Schematic diagram of the snow fence and the snow accumulation trend in the Control (C) and High (H) zones. Photographs showing (b) the bare ground, (c) pebbles covered with shallow snow in the C zone, and (d) snow depths of 20 cm (C zone) and 50 cm (H zone).

defined as the High zone (expressed hereafter as "H zone"), where the snow accumulation is strongly influenced by the fence (Fig. 2a). The C zone shows the natural snowfall because it is unaffected by the snow fence. In the H zone, the wind speed drops sharply because the air flow changes under the influence of the fence, producing eddies. Therefore, most of the snow is caught in the downwind drift of the H zone, and the snow depth beyond the H zone decreases noticeably. Figure 2b shows one of the snow fences and the bare ground of the C and H zones on either side of the fence. On 2 October 2017, most of the ground in the C zone was covered with snow shallow enough to distinguish large pebbles, whereas the H zone was covered with snow that was ~10 cm thicker (Fig. 2c). One month later (7 November 2017), we measured snow depths of 20 and 50 cm in the C and H zones, respectively (Fig. 2d).

For this study, five snow fences were installed in September 2017 perpendicular to the prevailing wind direction (WNW), which was determined based on wind records over two years: 1 October–31 December 2015 (Fig. 3a) and 1 October–31 December 2016 (Fig. 3b). Each fence was 1 m tall and 8 m long, and had regular holes of 4 cm diameter to allow the snow and wind to flow through. Every year the fences were dismantled at the

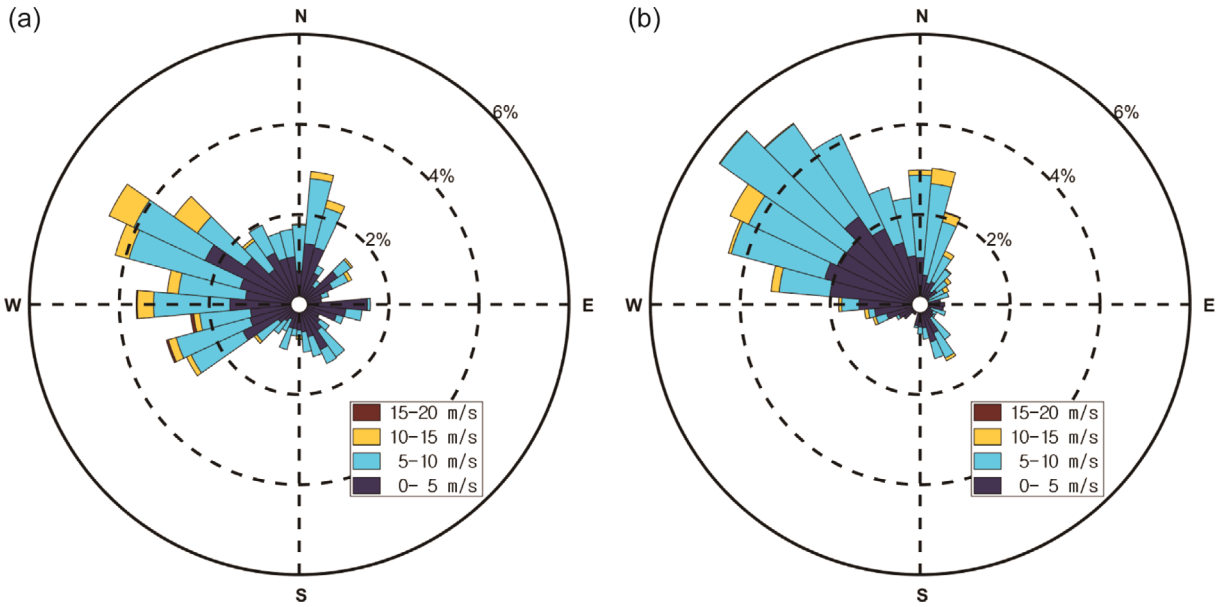

Fig. 3. Wind speed and direction in the survey area during the periods of 1 September to 31 December (a) 2015 and (b) 2016. Wind prevails in the WNW direction.

beginning of the thawing season (mid-June) to eliminate the effects of shade on the vegetation and were reinstalled in mid-September to manipulate the snow depth.

3. TEMPERATURE PROFILE AND DATA ACQUISITION

3.1. Temperature and Moisture Profiles

Cambridge Bay is covered with snow for about 250 days a year from October to May (McLennan et al., 2015). The 30-year average (1981–2010) temperature and snowfall are −13.9 °C and 80 cm, respectively. The lowest average temperature is −32.5 °C in February and the highest average is 8.9 °C in July, with the temperature difference reaching ~40 °C. The average temperature over the 20-year period 1991–2010 increased by 1.7 °C compared with the period 1961–1980.

Snow cover plays the most important role in controlling the ground temperature in permafrost terrain. Complicated relations exist between snow cover, air temperature, thermal conditions of the ground, active layer soil moisture, and vegetation. Figure 4 shows the daily air temperature timeseries for Period I (September 2017–August 2018) and Period II (September 2018–August 2019), which were collected from the automatic weather system at Cambridge Bay airport, 3 km away from the study site. The temperature during Period I was ~0 °C in the middle of September, and decreased gradually to the end of September, then fluctuated below −20 °C, with a minimum of approximately −40 °C from November to March of the following year (Fig. 4a). The temperature increased rapidly after April, exceeding 0 °C in early June, with a maximum of 10 °C in the middle of July, followed by a gradual decrease again from August. Period II (Fig. 4b) shows a similar pattern to Period I. The average temperatures during Period I and Period II are −13.5 (14.8) °C and −13.4 (15.3) °C, respectively and their difference is not significant ($p > 0.05$). Monthly average temperatures over the thawing season of June, July, and August are 2.0 (4.7) °C, 8.3 (2.4) °C, and 4.9 (2.4) °C, respectively for Period I, and 2.9 (3.6) °C, 8.0 (2.2) °C, and 8.1 (2.8) °C, respectively for Period II, with only slight differences in June and July ($p > 0.05$), whereas the difference in August is significant ($p < 0.05$). The aforementioned p-value is a measure of the probability that an observed difference could have occurred just by random chance. The lower the p-value, the greater the statistical significance of the observed difference.

The ground temperature and moisture were measured using the METER-Teros11 at depths of 5 and 20 cm in the C and H zones (Fig. 5). The ground temperature changed much more at 5 cm than at 20 cm because of the influence of the air temperature during both the thaw and freezing seasons (Fig. 5a). During the winter, the ground temperature in the H zone was ~10 °C higher than that of the C zone because of insulating snow cover, which has low thermal conductivity. This ground warming effect was

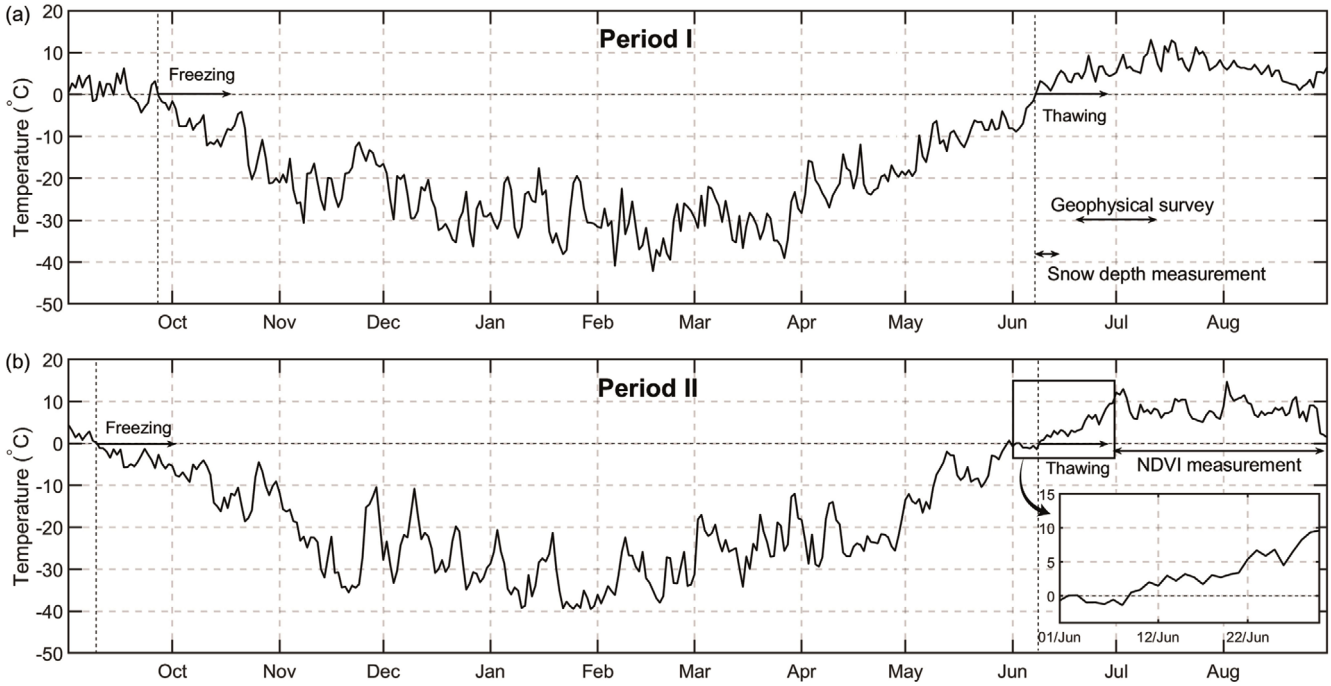

Fig. 4. Daily air temperature records for (a) Period I (1 September 2017 to 31 August 2018) and (b) Period II (1 September 2018 to 31 August 2019). The geophysical survey and snow-depth measurements were conducted during Period I, whereas the NDVI measurements took place during Period II. In both Periods I and II, thawing starts in early June.

https://doi.org/10.1007/s12303-021-0021-7

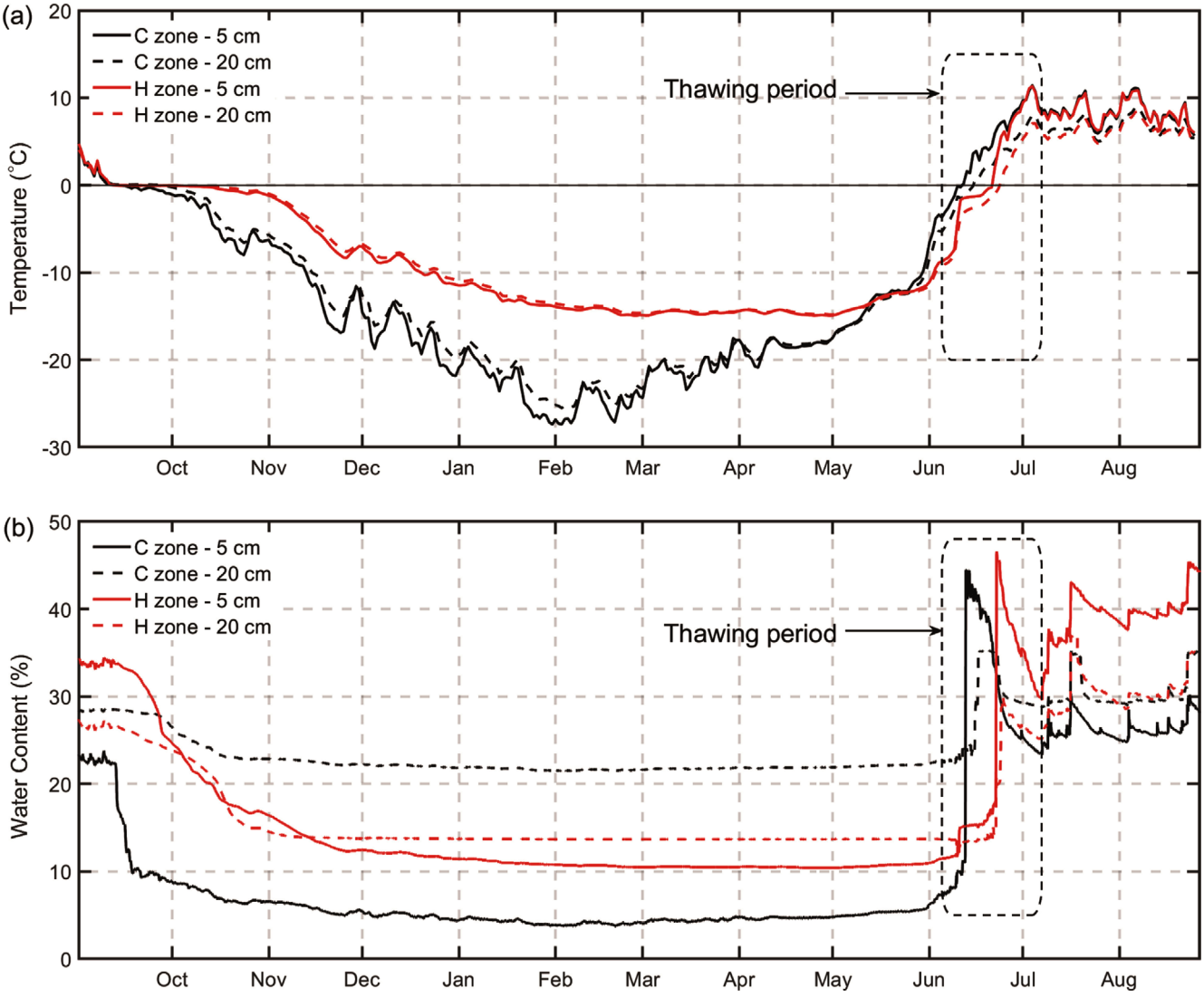

Fig. 5. Daily profiles of (a) ground temperature and (b) soil moisture, which are measured by the loggers at depths of 5 and 20 cm in the C and H zones. Note that the temperature in the C zone is higher than in the H zone and there is a rapid increase of moisture content in the early thawing period. Note that the temperature in the C zone is higher than in the H zone and the temperatures at 5 cm depth reach zero on 12 June (C zone) and 22 June (H zone). There is a rapid increase of moisture contents (from 11% to 44%) in the C zone and H zone (from 18% to 45%) on those dates.

also inferred from the excrement of lemmings beneath the H zone, who built nests under the thick snow to insulate themselves over the winter. Throughout most of the subzero degree window, the temperature at 20 cm depth was slightly higher than that at 5 cm depth, due to the geothermal gradient.

Soil moisture (Fig. 5b) in the C zone at 5 cm depth increased rapidly from 11% to 44% on 12 June, whereas that at 20 cm depth increased from 25% to 35% on 15 June. In the H zone, soil moisture at 5 cm increased from 18% to 45% on 22 June, whereas that at 20 cm depth increased from 15% to 30% one day later, on 23 June. This sudden increase in soil moisture reflects the transition of ice to water. Based on this observation, the ground thawed 10 days earlier in the C zone than in the H zone. Comparing the thawing time up to 20 cm depth, it took 3 days for the soil to thaw from 5 to 20 cm in the C zone and one day in the H zone. This thawing-time difference is explained by the air temperature profile (Fig. 4), which shows that when the H zone thawed, the air temperature was approximately 5 °C higher than when the C zone thawed. The ALT would be almost the same in the C and H zones after some time.

Before the thaw, the temperature is higher in H zone than in C zone, and at 20 cm depth than at 5 cm depth. Those patterns reversed, as the snowmelt season approached (early June) (Fig. 5a). This was most likely because of the reflection of solar radiation and the release of latent heat during the thaw, which is well supported by the rapid increase of water content in the

middle of June (Fig. 5b) and the higher NDVI in the C zone (see Fig. 11). After the snow had completely melted, the temperatures of the C and H zones were almost equal due to the bare ground absorbing the same amount of solar radiation in both zones.

When the freezing period began, the temperature at 5 cm depth dropped below zero much faster than at 20 cm depth. An analogous pattern also appeared during the thaw at the beginning of June 2019, in that the 5 cm-depth temperature increased more rapidly to zero than the 20 cm-depth temperature and attained higher values. The temperature gradient appeared to be higher during the thawing period (June) than in the freezing period (October).

The soil temperature in the C zone reached zero earlier than in the H zone during both the thawing and freezing periods. Considering the air temperature during the geophysical survey period (18 June–8 July 2018), the lower ground temperature in the H zone compared with the C zone was probably caused by the presence of thick, widespread snow cover behind the fence, resulting in high reflection of solar radiation and smaller ambient temperature effects.

3.2. Geophysical Survey

A number of geophysical properties are significantly altered when water changes phase. Surface-based geophysical methods are a cost-effective approach to active layer mapping and characterization, especially when repeated through time to monitor the changing ground conditions.

To delineate the subsurface structure and to monitor the active layer around the snow fence in the permafrost terrain, two geophysical methods were undertaken at the same location during the thawing period (23 June–8 July 2018). We used GPR for the shallower targets and ERT for the deeper targets.

GPR data were collected using a MALA system with 800, 400, 250 MHz antennas for three objectives. The radar velocity of polar snow is greater than that of ground due to low dielectric constant (Reynolds, 2011). Vertical resolution can be taken as one-quarter of the wavelength (= radar velocity/frequency) of incident radiation. Accordingly, we selected the higher frequency 800 MHz for enhancing the resolution of the shallow target (snow depth) and the lower frequency 250 MHz for mapping the deeper target (the base of active layer). Bistatic system 400 MHz antenna was selected for CMP velocity sounding because there are separate antennas for transmitting and receiving. (1) To examine the snow depth, a survey using an 800 MHz antenna was conducted at a series of times during the thawing period (5, 8, and 10 June 2018) over a 50 m line across the snow fence. The snow on the ground on 5 June was hard and comfortable to work on. However, every step of the walk on 8 June made a deep mark as the snow began to melt. On 10 June, the snow melted so much that it turned into slush. At that time, we deployed a 10 m shorter line, recognizing that much of the snow in the C zone had melted. (2) To construct the depth-velocity profile, the common mid-point (CMP) shooting method was applied using a 400 MHz antenna on 28 June. (3) To investigate the active-layer thickness variation, a total of five surveys were conducted on a line using a 250 MHz antenna from 18 June to 8 July 2018.

The ERT surveys were performed using the ABEM LS Terrameter 2 employing the Wenner array with 64 electrodes, an electrode spacing of 1 m, 2–4 stack numbers, and a 20 mA current. The Wenner array was chosen because it is suitable for shallower targets, providing better vertical and horizontal resolution. The ERT data were collected every four days from 18 June to 8 July 2018, immediately after the snow of the H zone had completely melted.

3.3. Plant Survey

Plant coverage was determined in two plots (40 × 40 cm) within each zone on either side of five snow fence replicates in 2018. The vascular plant species were assigned to deciduous shrubs, graminoids, and forbs using a previous classification of International Tundra Experiment species (Elmendorf et al., 2012). Plant phenology was determined using the NDVI. The coverage and activity of vegetation depend on the snow depth and have impacts on the thermal properties of soil and on geophysical images.

In this study, we used a miniaturized hyperspectral camera, Specim IQ (Specim Ltd., Oulu, Finland) to quantify vegetation conditions between the C and H zones. The sensor is designed as a mobile, handheld, and stand-alone scanner with an integrated operating system, which controls and measures spectral reflectance from 400 to 1000 nm using 204 spectral bands of 7 nm spectral resolution. The number of pixels in each scan line is 512, and the sensor scans 512 lines, so the final output image provides 512 pixels × 512 pixels × 204 channels (Behmann et al., 2018). A nearly 100% reflective white reference panel (also known as Spectralon), which is located next to the target, is often used to quantitatively measure spectral reflectance under different illumination conditions and to determine the best integration time under the current illumination conditions.

We collected ground-based hyperspectral data weekly from 28 June to 7 September 2019. Two hyperspectral images were obtained in each zone of the five snow fence replicates, and the total number of images was 198 for this experiment. To calculate the NDVI for the target area, we defined a region of interest as shown in Figure 6a. We first defined a target area (i.e., a rectangular boundary of 40 × 40 cm) and placed a white reference panel outside the target area. Figure 6b shows the spectral reflectance curves derived from the hyperspectral image. As shown, the

https://doi.org/10.1007/s12303-021-0021-7

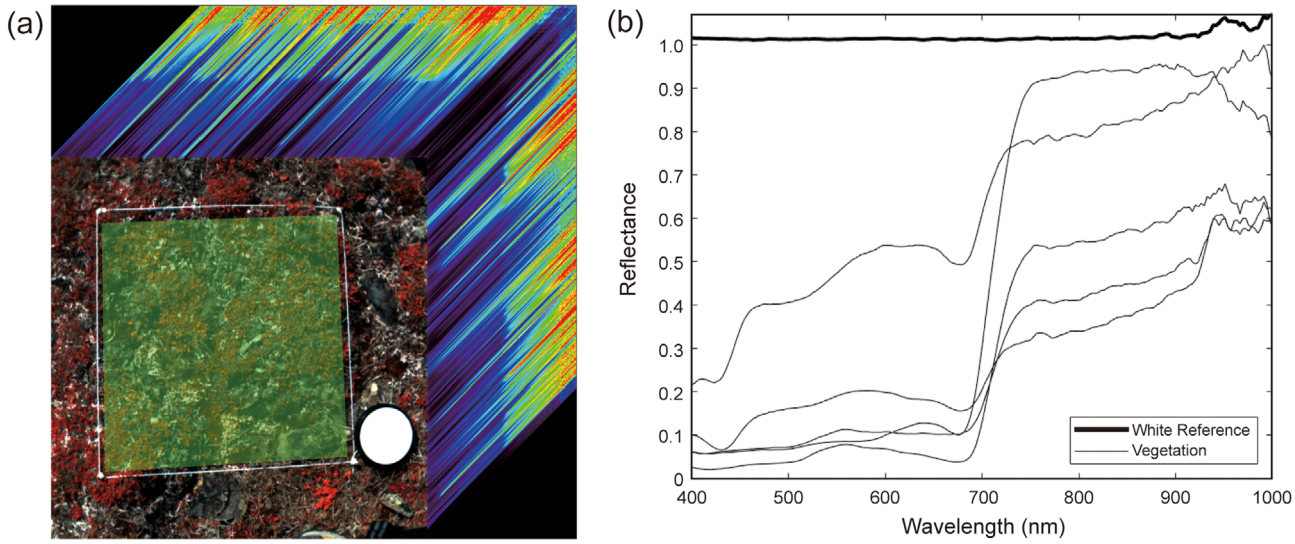

Fig. 6. (a) Sample of a 512 × 512 3D hyperspectral image cube with 204 spectral bands. The green shaded area is a region of interest (ROI) and the white reference panel in the lower right corner is used for reflectance conversion. (b) Spectral reflectance curves for the white reference panel and vegetation samples from the hyperspectral image.

reflectance samples from the white reference panel have a reflectance of nearly one, and the vegetation samples show the distinctive spectral signature of green vegetation, which has high reflectance in the near-infrared (NIR; 800 nm for the calculation) compared with the visible band (670 nm for the calculation). This indicates that the sensor correctly records reflectance values. Although reflectance values in the 900–1000 nm range are noisy due to the low signal level and atmospheric absorption in this range, these bands are unnecessary for NDVI calculations.

4. RESULTS AND INTERPRETATION

4.1. Geophysical Mapping of the Active Layer

Figure 7 shows the GPR sections and the snow-depth change on different days. Because we were unable to implement the CMP method on those days, the snow depth was calculated using a radar velocity of 0.2 m/ns, which is representative for polar snow (Reynolds, 2015). The snow depth thickened from the C

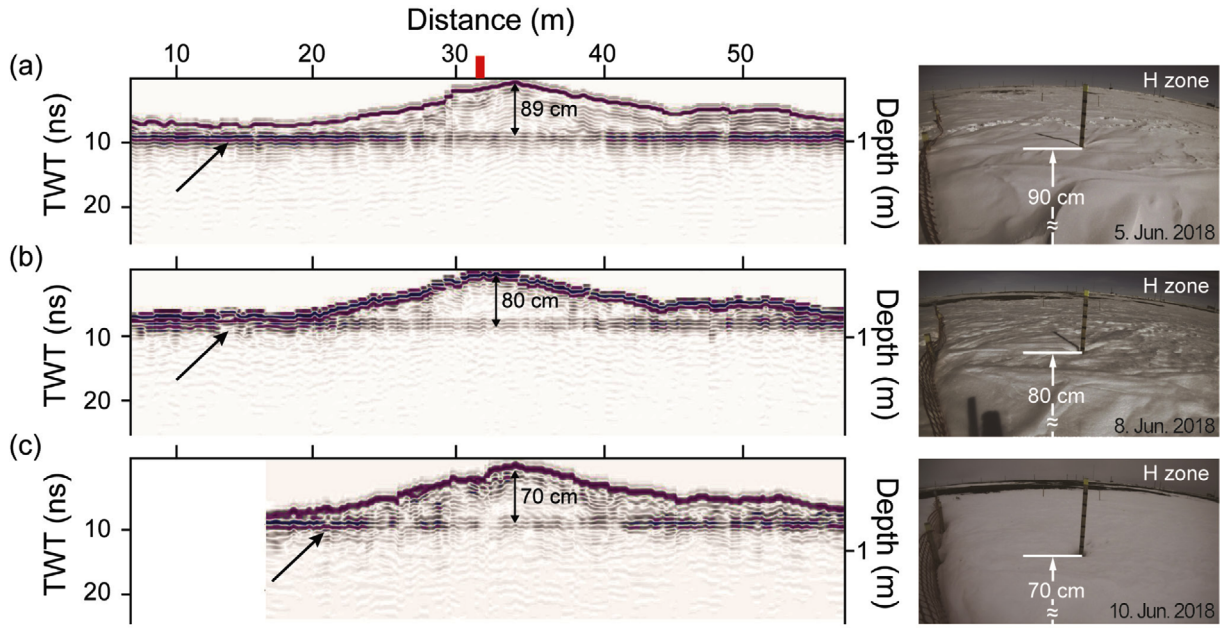

Fig. 7. Snow depths estimated in the GPR section are well correlated with the snow heights measured on (a) 5 June 2018, (b) 8 June 2018, and (c) 10 June 2018. Slight differences in (b) and (c) are probably caused by the increase of water content as the snow melted. The red tick indicates the position of the snow fence, the arrow indicating the ground reflections. TWT means two-way travel time.

zone to the H zone, reaching a maximum thickness of 90 cm on 5 June (Fig. 7a). Three days later (8 June), the structure was largely similar, but with a slightly lower maximum snow height of 80 cm (Fig. 7b). The ground reflections were often lacking in lateral consistency and phase coherence, which was probably caused by the snow melting on the surface. The radar signal was deteriorated due to the water from melting snow. The survey two days later (10 June) indicated that snow melting was in progress, particularly in the C zone, where the snow thickness reduced to 70 cm (Fig. 7c). The snow depths calculated from the GPR data correspond well to the heights shown in the photo on the right side of Figure 7a. However, the correspondence was decreased on 8 and 10 June 2018. This was caused by the reduced velocity, indicated by the large values of dielectric constants, which resulted from the increased water content as the snow melted. The radar velocity using the measured snow thickness was calculated as 0.19 m/ns and 0.14 m/ns on 8 and 10 June, respectively.

We now investigate the variation of the ALT using five time-lapse radargrams from 18 June to 8 July 2018 (Fig. 8a). Depth conversion was applied on the basis of radar velocity spectra, which were provided by the CMP shooting conducted on 28

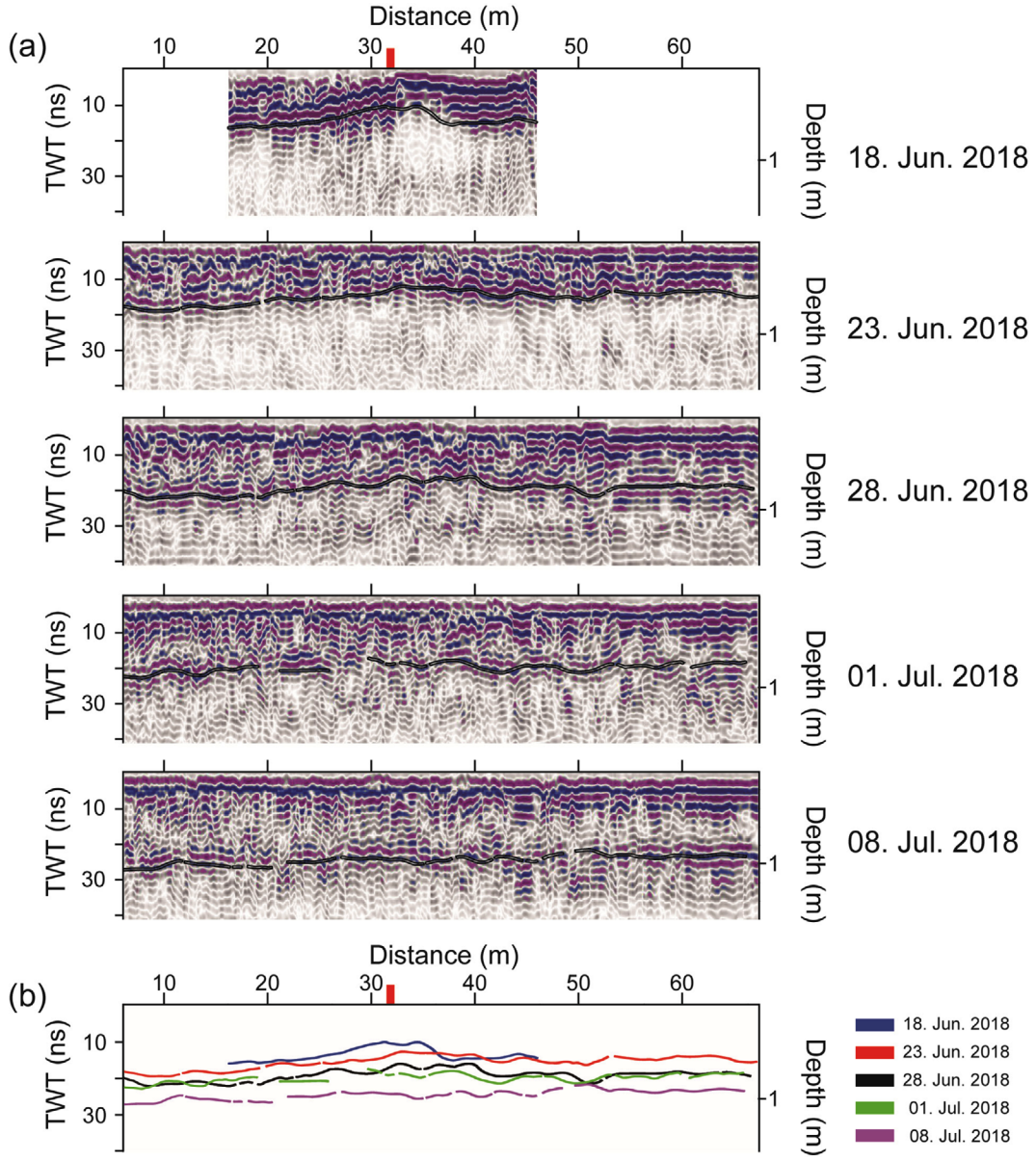

Fig. 8. (a) Time-lapse radargram representing the thickening of the active layer with time and (b) selected times for the base of the active layer. In the early thawing period (23 June), the active layer is much thicker in the C zone than in the H zone. On 8 July, the thickness appears to be almost the same (~1 m deep). The red tick indicates the position of the snow fence and the black drawn lines represent the base of the active layer. TWT means two-way travel time.

https://doi.org/10.1007/s12303-021-0021-7

June 2018. The depth conversion calculation was based on an ALT velocity of 0.078 m/ns estimated from the velocity spectra.

The thickening of the active layer with time is clearly shown from measurements taken at the base of the active layer at selected times (Fig. 8b). The base of the active layer was determined by connecting the peak amplitude trace-by-trace with semi-auto picking module in the REFLEXW processing package. During the early stage of the thawing season, the active layer of the C zone was much thicker (~0.3 m) than that of the H zone because the thinner snow cover of the C zone disappeared faster, and thus the temperature of the subsurface increased more rapidly under the increased solar radiation. The travel-time difference between the C and H zones decreased with time. When the snow completely melted (8 July), the ALTs of the C and H zones appeared to be almost the same. The base of the active layer lowered gradually and flattened with time, in contrast with discrete misalignments due to gravels scattered at shallow depth (Fig. 9a). The ALT (or the distance to the permafrost) of approximately 1 m is well explained by the depth of the frozen soil and by the profiles indicating increased moisture content and a temperature of 0 °C at 1 m depth (Fig. 9b). This ALT, estimated and observed in the geophysical survey and digging data, agrees well with the average active layer depth in the CHARS Greater Ecosystem (McLennan et al., 2015). The active layer thickened with time, increasing from 0.5 m on 18 June to 1 m on 8 July. This was caused by the ice melting with the increasing ground temperature.

Figure 10 shows the time-lapse electrical resistivity structures over 13 days (23 June–5 July 2018). The data were collected two days after the snow and ice had completely melted. The topmost section collected on 23 June shows the freezing surface (high resistivity) in the H zone and the underground partially melted (low resistivity) in the C zone. The approximately 1 m-thick low resistivity zone beyond the distance of 45 m was probably caused by infiltrating water from the melting snow. Over time, the electrical resistivities at shallow depths decreased gradually throughout the whole section, but they decreased most significantly in the H zone. The low resistivity zone (~200 Ωm) below the approximately 1.5 m-thick active layer is most likely the unfrozen talik, which is a layer of unfrozen ground often occurring underneath or around shallow thermokarst lakes (Frédéric et al., 2016). We interpret the high-resistivity zone (> 1000 Ωm) at the bottom to be the permafrost or bedrock, which has a gentle slope toward the H zone.

Like the radargram (Fig. 8), the electrical resistivity section shows that the active layer of the H zone is more resistive than the C zone in the early thawing stage. This is because the ground beneath the surface of the H zone was still frozen, whereas that of the C zone was partially thawed. This phenomenon contradicts the general principle that the more snow that accumulates, the warmer the ground is below. However, it is supported by the underground temperature profile showing a steep temperature gradient (Fig. 5a) and large NDVI values for the C zone (Fig. 11) in the early stage. After three weeks of snow-free conditions (from the middle of July), the NDVI became higher in the H zone than in the C zone because the active vegetation received a higher amount of infiltrated water during the high-temperature period.

4.2. Plant Responses to Snow Depth

Snow depth did not make any difference to plant composition

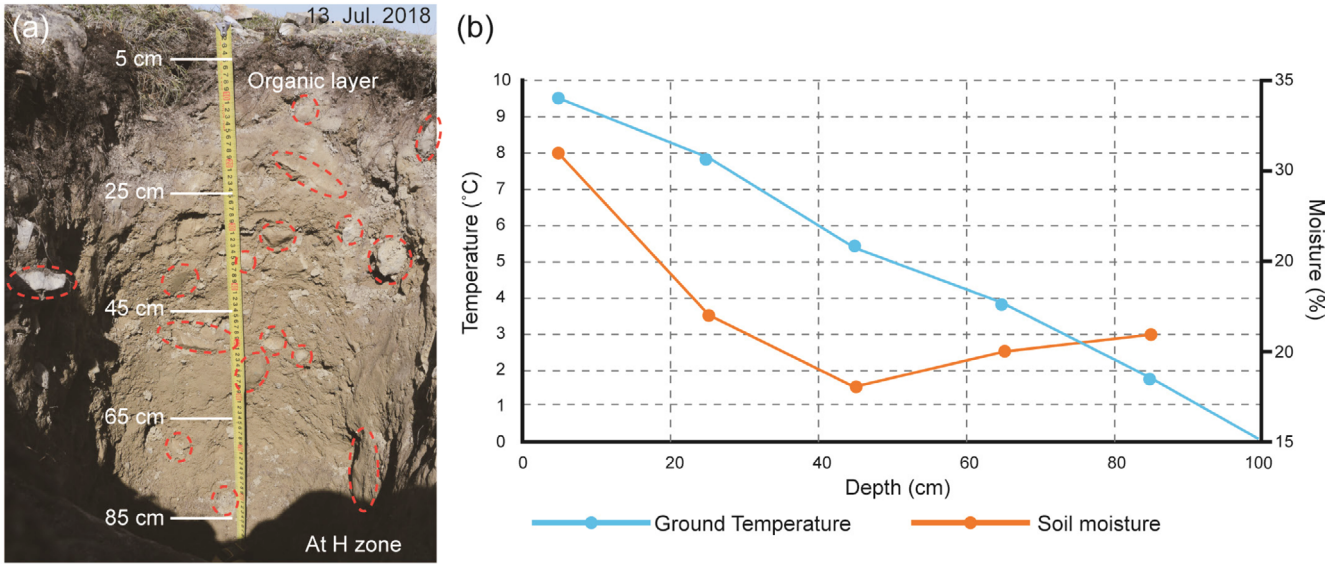

Fig. 9. (a) A photograph of gravel-rich soil (indicated by the red ellipses) observed during the logging. (b) Frozen soil with gravel is encountered at 1 m depth with a temperature of 0 °C and a moisture content of ~23% on 13 July, respectively.

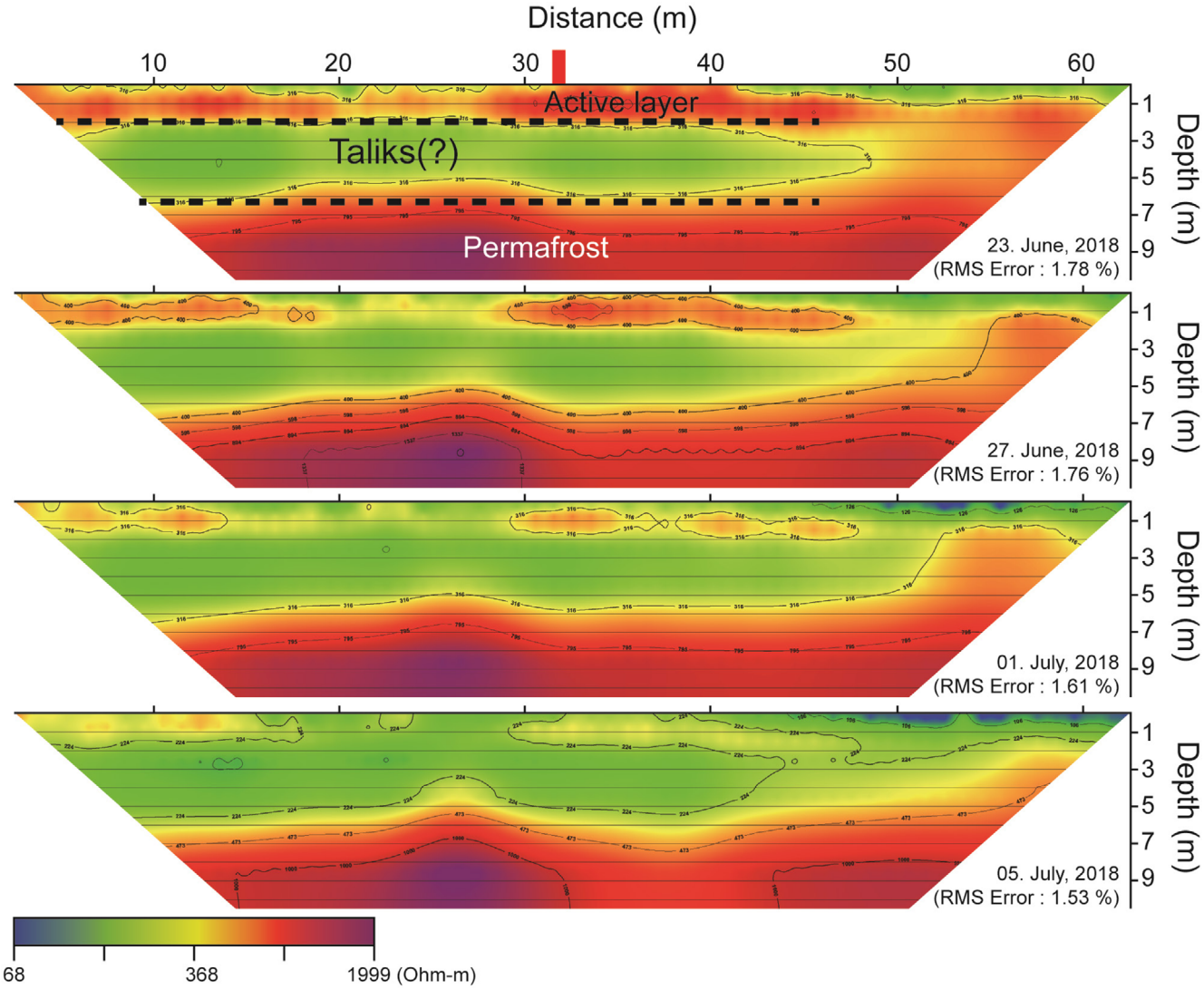

Fig. 10. Time-lapse electrical resistivity tomography (ERT) showing the decrease of electric resistivity of the active layer with time, the unfrozen low-resistive taliks, and high-resistive permafrost. The red tick indicates the position of the snow fence. RMS error is root-mean-square error between the observed data and the calculated data provided in the process of achieving the resistivity tomography.

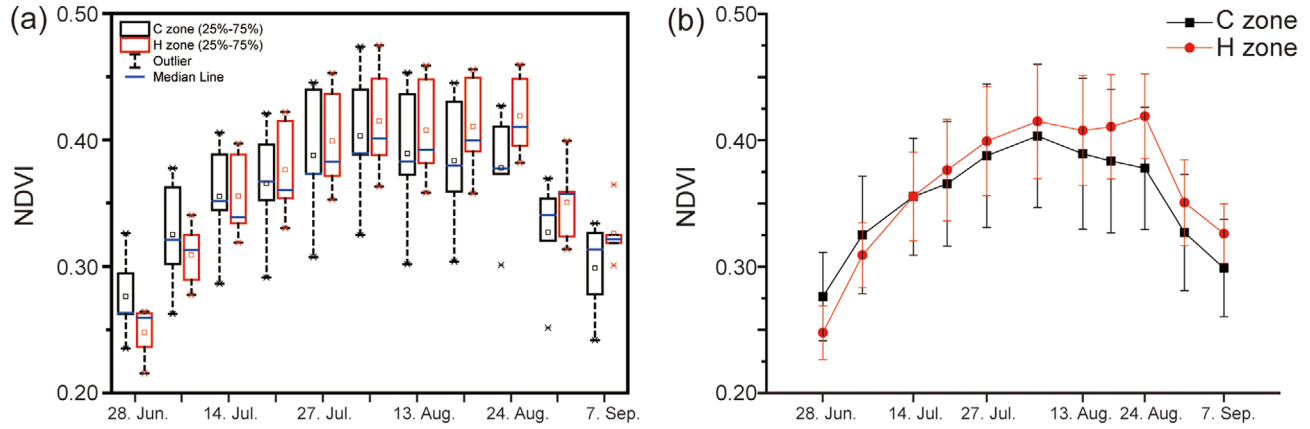

Fig. 11. (a) The range of NDVI values during the plant growing season in 2019 for the C and H zones. Small squares in the middle of the box indicate the average values. (b) Profiles of the mean (solid shapes) and standard deviation (vertical bars) of NDVI values (the number of samples used to calculate the mean and standard deviation was five).

https://doi.org/10.1007/s12303-021-0021-7

Table 1. Plant compositions in survey plots

	C		H	
	Mean	SD	Mean	SD
Deciduous Shrubs (%)	40.4	11.9	35.0	7.0
Graminoids (%)	16.9	10.0	14.9	1.3
Forbs (%)	4.9	3.6	5.5	5.2
Mosses (%)	6.9	5.6	10.8	9.3
Lichens (%)	17.4	8.1	8.0	3.5
Total Vascular Plants (%)	62.2	13.4	55.4	9.8

Total vascular plants are the sum of deciduous shrubs, graminoids, and forbs.

(Table 1). The short one-year period during which the snow fence was operating, along with the highly variable distribution of tundra vegetation, might have made it difficult to discern the effects of the snow fence. In both the C and H zones, deciduous shrubs showed the highest coverage, followed by graminoids and forbs. Mosses, lichens, and non-vascular plants covered ~20% of the plots. The coverage of lichens was higher in the C zone, whereas mosses showed a higher coverage in the H zone.

Although there were some outliers at the end of the growing season (Fig. 11a), the average NDVI values steadily increased, reaching a maximum in early August, and then decreasing from the end of August (Fig. 11b). There were no significant differences in the NDVI between the C and H zones because of the large amount of gravel and rocks on the soil surface, which resulted in high spatial variability of vegetation coverage in the measurement locations. Despite there being no statistical difference, we found that the NDVI values in the C zone were higher at the beginning of the growing season than that in the H zone. However, the average value of the NDVI in the H zone was higher than that in the C zone from the end of July, and this pattern was maintained until the end of the growing season. The shallow snow cover in the C zone exposed the soil surface earlier than in the H zone, and this allowed plants to start growing earlier. In the H zone, the plants began growing later than in the C zone due to the longer period needed to melt the higher volume of accumulated snow. However, this larger amount of snow might also have provided much-needed water to plants during the growing period of this dry tundra ecosystem.

5. CONCLUSIONS

We have mapped the variation of the ALT through time-lapse GPR and ERT data collected across a snow fence at a permafrost terrain in Cambridge Bay, Nunavut, Canada. The seasonal thawing of the active layer was associated with a lowered and flattened radar event and a slower resistivity decrease.

High resolution radargrams collected in the thawing season indicate that the ALT increased with time, showing a maximum depth of ~1 m in the middle of July, coinciding with the highest temperature of the year. In addition, radar reflection events provided information about the snow depth, which corresponded well to the actual snow heights measured through surveys. The ERT mapping of the deeper structures showed the active layer and the underlying low resistivity zone of taliks, as well as the high resistivity of the permafrost.

Time-lapse geophysical structures across the snow fence (i.e., in the C and H zones) were investigated in terms of air and ground temperature, ground moisture, NDVI-based vegetation activity, snow cover, and snow depth. In the early thawing period, the active layer of the C zone was thicker than that of the H zone because the surveys were carried out in the absence of snow cover and there was no insulating snow effect. Meanwhile, the ground temperature of the C zone was already high, as the snow cover there was thinner and able to melt more quickly, allowing direct solar radiation to reach the surface. This effect was also confirmed by the higher NDVI values in the C zone than in the H zone at the beginning of the growing season. The plants in the C zone grew earlier than in the H zone because the shallow snow cover disappeared more quickly. As the available nitrogen increases with temperature under deeper snow cover, vegetation becomes more active; therefore, differences in NDVI values and organic-layer thicknesses between the C and H zones are expected to increase in the future.

More carefully planned high resolution seismic surveys (MASW-based S-wave profile and refraction tomography) in both the freezing and thawing periods, as well as appropriate analyses of soil properties, should further improve imaging and understanding of the physical behavior of the active layer in a permafrost environment.

ACKNOWLEDGMENTS

This research was supported by a National Research Foundation of Korea Grant from the Korean Government (MSIT; the Ministry of Science and ICT NRF-2021M1A5A1065425) (KOPRI-PN21011) and the Korea Polar Research Institute project PE21080.

REFERENCES

Barendregt, R.W., Vincent, J.S., Irving, E., and Baker, J., 1998, Magnetostratigraphy of Quaternary and late Tertiary sediments on Banks Island, Canadian Arctic Archipelago. Canadian Journal of Earth Sciences, 35, 147–161.

Behmann, J., Acebron, K., Emin, D., Bennertz, A., Matsubara, S., Thomas, S., Bohnenkamp, D., Kuska, M.T., Jussila, J., Salo, H., Mahlein, A., and Rascher, U., 2018, Specim IQ: evaluation of a new, miniaturized handheld hyperspectral camera and its application for plant pheno-

typing and disease detection. Sensors, 18, 441.

Blanc-Betes, E., Welker, J.M., Sturchio, N.C., Chanton, J.P., and Gonzalez-Meler, M.A., 2016, Winter precipitation and snow accumulation drive the methane sink or source strength of Arctic tussock tundra. Global Change Biology, 22, 2818–2833.

Briggs, M.A., Campbell, S., Nolan, J., Walvoord, M.A., Ntarlagiannis, D., Day-Lewis, F.D., and Lane, J.W., 2017, Surface geophysical methods for characterising frozen ground in transitional permafrost landscapes. Permafrost and Periglacial Processes, 28, 52–65.

Brown, J., Ferrians Jr., O.J., Heginbottom, J.A., and Melnikov, E.S., 1997, Circum-Arctic map of permafrost and ground-ice conditions. Circum-Pacific Map 45, U.S. Geological Survey, Reston. https://doi.org/10.3133/cp45

Dolbinski, W., 2009, Geophysical methods in research of permafrost in the tetra mountains and northern Scandinavia. Landform Analysis, 10, 26–32.

Elmendorf, S.C., Henry, G.H.R., Hollister, R.D., Björk, R.G., Boulanger-Lapointe, N., Cooper, E.J., Cornelissen, J.H.C., Day, T.A., Dorrepaal, E., Elumeeva, T.G., Gill, M., Gould, W.A., Harte, J., Hik, D.S., Hofgaard, A., Johnson, D.R., Johnstone, J.F., Jónsdóttir, I.S., Jorgenson, J.C., Klanderud, K., Klein, J.A., Koh, S., Kudo, G., Lara, M., Lévesque, E., Magnússon, B., May, J.L., Mercado-Dı´az, J.A., Michelsen, A., Molau, U., Myers-Smith, I.H., Oberbauer, S.F., Onipchenko, V.G., Rixen, C., Martin Schmidt, N., Shaver, G.R., Spasojevic, M.J., Þórhallsdóttir, .E., Tolvanen, A., Troxler, T., Tweedie, C.E., Villareal, S., Wahren, C.-H., Walker, X., Webber, P.J., Welker, J.M., and Wipf, S., 2012, Plot-scale evidence of tundra vegetation change and links to recent summer warming. Nature Climate Change, 2, 453–457.

Erji, D., Lin, Z., Tonghua, W., Ren, L., Guangyang, Y., Xiaodong, W., Wangping, L., Yongliang, J., Guojie, H., Yongping, Q., Zhiwei, W., Defu, Z., and Guangyue, L., 2016, The relationship between the ground surface layer permittivity and active-layer thawing depth in a Qinghai-Tibetan Plateau permafrost area. Cold Regions Science and Technology, 126, 55–60.

Farzamian, M., Vieira, G., Santos, F.A.M., Tabar, B.Y., Hauck, C., Paz, M.C., Bernardo, I., Ramos, M., and Pablo, M.A., 2020, Detailed detection of active layer freeze-thaw dynamics using quasi-continuous electrical resistivity tomography (Deception Island, Antarctica). The Cryosphere, 14, 1105–1120.

Frédéric, B., Daniel, F., Michel, P., Vincent, B., Reinhard, P., and Isabelle, L., 2020, Thermokarst lake inception and development in syngenetic ice-wedge polygon terrain during a cooling climatic trend, Bylot Island (Nunavut), eastern Canadian Arctic. The Cryosphere, 14, 2607–2627.

Frédéric, B., Lauren, A.M., Kevin, W.T., Joshua, R.T., Andrew, S.M., Boris, K.B., Jennifer, K., Roland, I.H., Reinhard, P., and Brent, B.W., 2016, Paleolimnology of thermokarst lakes: a window into permafrost landscape evolution. Arctic Science, 3, 91–117.

Harris, S.A., French, H.M., Heginbottom, J.A., Johnston, G.H., Ladanyi, B., Sego, D.C., and van Everdingen, R.O., 1988, Glossary of permafrost and related ground-ice terms. Technical Memorandum No. ACGR-TM-142, National Research Council of Canada. Associate Committee on Geotechnical Research. Permafrost Subcommittee, Ottawa, 159 p. https://doi.org/10.4224/20386561

Harrison, J.C., Christie, R.L., Rainbird, R.H., and Ford, A., 2013, Geology, tectonic assemblage map of the Cambridge Bay area, southeastern Victoria Island, Nunavut (1:500,000). Canadian Geoscience Map No. 78, Geological Survey of Canada, Ottawa. https://doi.org/10.4095/292813

Heginbottom, J.A, Dubreuil, M.A, and Harker, P.T, 1995, Canada, permafrost (1:7,500,000). The National Atlas of Canada, Natural Resources Canada, Geomatics Canada, MCR Series No. 4177, Natural Resources Canada, Ottawa. https://doi.org/10.4095/294672

Hinkel, K.M. and Hurd Jr., J.K., 2006, Permafrost destabilization and thermokarst following snow fence installation, Barrow, Alaska, U.S.A. Artic, Antarctic, and Alpine Research, 38, 530–539.

Hugelius, G., Strauss, J., Zubrzycki, S., Harden, J.W., Schuur, E.A.G., Ping, C.-L., Schirrmeister, L., Grosse, G., Michaelson, G.J., Koven, C.D., O'Donnell, J.A., Elberling, B., Mishra, U., Camill, P., Yu, Z., Palmtag, J., and Kuhry, P., 2014, Estimated stocks of circumpolar permafrost carbon with quantified uncertainty ranges and identified data gaps. Biogeosciences, 11, 6573–6593.

John, S., 1980, Drumlins and large-scale flutings related to glacier folds. Arctic and Alpine Research, 12, 287–298.

Lafreniere, M.J., Laurin, E., and Lamoureux, S.F., 2012, The impact of snow accumulation on the active layer thermal regime in high arctic soils. Vandose Zone Journal, 12, 1–13. https://doi.org/10.2136/vzj2012.0058

McLennan, D., Wagner, I., Turner, D., McKillop, R., MacKenzie, W., Meidinger, D., Bennett, B., Obst, J., Buddle, C., Navarro, N., Kafle, P., Sullivan, J., Tomaselli, M., Rautio, M., Power, M., Culp, J., Wrona, F., Chaves-Barquero, L., Luong, K., Knapp, C., Mundy, C. J., Hanson, M., and Wong, C., 2015, Towards the development of the Canadian High Arctic Research Station (CHARS) as a centre of science and technology in Canada and the Circumpolar North: regional, social and ecological context, baseline studies, and monitoring pilots. Report, Polar Knowledge Canada, 135 p. https://above.nasa.gov/Documents/CHARS_Science_Summary_June_2015_DRAFT.pdf [Accessed on 5 July].

O'Neill, H.B. and Burn, C.R., 2017, Impacts of variations in snow cover on permafrost stability, including simulated snow management, Dempster Highway, Peel Plateau, Northwest Territories. Arctic Science, 3, 150–178.

Osterkamp, T.E. and Burn, C.R., 2003, Permafrost. In: Holton, J.R., Pyle, J., and Curry, J.A. (eds.), Encyclopedia of Atmospheric Sciences. Academic Press, Oxford, p. 1717–1729. https://doi.org/10.1016/B0-12-227090-8/00311-0

Osterkamp, T.E., Jurick, R.W., Gislason, G.A., and Akasofu, A.I., 1980, Electrical resistivity measurements in permafrost terrain at the Engineer Creek road cut, Fairbanks, Alaska. Cold Regions Science and Technology, 3, 277–286.

Pries, C.E.H., Schuur, E.A.G., Natali, S.M., and Crummer, K.G., 2016, Old soil carbon losses increase with ecosystem respiration in experimentally thawed tundra. Nature Climate Change, 6, 214–218.

Reynolds, J.M., 2011, An Introduction to Applied and Environmental Geophysics (2nd edition). Wiley-Blackwell, Chichester, 710 p.

Schuur, E.A.G., McGuire, A.D., Schädel, C., Grosse, G., Harden, J.W., Hayes, D.J., Hugelius, G., Koven, C.D., Kuhry, P., Lawrence, D.M., Natali, S.M., Olefeldt, D., Romanovsky, V.E., Schaefer, K., Turetsky, M.R., Treat, C.C., and Vonk, J.E., 2015, Climate change and the perma-

frost carbon feedback. Nature, 520, 171–179.

Storrar, R. and Stokes, C.R., 2007, A glacial geomorphological map of Victoria Island, Canadian Arctic. Journal of Maps, 3, 191–210, https://doi.org/10.1080/jom.2007.9710838

Taylor, A.E., Wang, K., Smith, S.L., Burgess, M.M., and Judge, A.S., 2006, Canadian Arctic permafrost observations: detecting contemporary climate change through inversion of subsurface temperature time series. Journal of Geophysical Research, 111, B02411. https://doi.org/10.1029/2004JB003208

Wang, X., Wang, T., Guo, H., Liu, D., Zhao, Y., Zhang, T., Liu, Q., and Piao, S., 2017, Disentangling the mechanisms behind winter snow impact on vegetation activity in northern ecosystems. Global Change Biology, 24, 1651–1662.

Wipf, S. and Rixen, C., 2010, A review of snow manipulation experiments in Arctic and alpine tundra ecosystems. Polar Research, 29, 95–109.

Woo, M.K., 2012, Permafrost Hydrology. Springer, Hamilton, 564 p.